Accepted Manuscript

Towards a subcutaneous optical biosensor based on thermally hydrocarbonised porous silicon

Wing Yin Tong, Martin J. Sweetman, Ezzat R. Marzouk, Cara Fraser, Tim Kuchel, Nicolas H. Voelcker

PII: S0142-9612(15)00796-6

DOI: 10.1016/j.biomaterials.2015.09.045

Reference: JBMT 17095

To appear in: *Biomaterials*

Received Date: 10 June 2015

Revised Date: 28 September 2015

Accepted Date: 29 September 2015

Please cite this article as: Tong WY, Sweetman MJ, Marzouk ER, Fraser C, Kuchel T, Voelcker NH, Towards a subcutaneous optical biosensor based on thermally hydrocarbonised porous silicon, *Biomaterials* (2015), doi: 10.1016/j.biomaterials.2015.09.045.

This is a PDF file of an unedited manuscript that has been accepted for publication. As a service to our customers we are providing this early version of the manuscript. The manuscript will undergo copyediting, typesetting, and review of the resulting proof before it is published in its final form. Please note that during the production process errors may be discovered which could affect the content, and all legal disclaimers that apply to the journal pertain.

ACCEPTED MANUSCRIPT

Towards a subcutaneous optical biosensor based on thermally hydrocarbonised porous silicon

Wing Yin Tong[1], Martin J. Sweetman[1], Ezzat R. Marzouk[2&3], Cara Fraser[4], Tim Kuchel[4], Nicolas H. Voelcker[1+]

[1]ARC Centre of Excellence in Convergent Bio-Nano Science and Technology, Mawson Institute, University of South Australia, South Australia, Australia

[2]Centre for Environmental Risk Assessment and Remediation, University of South Australia, South Australia, Australia

[3] Faculty of Environmental Agricultural Sciences, Suez Canal University, North Sinai, Egypt

[4]South Australian Health and Medical Research Institute, South Australia, Australia

+Correspondences should be sent to:
Nicolas H. Voelcker (Nico.Voelcker@unisa.edu.au)

Abstract

Advanced biosensors in future medicine hinge on the evolvement of biomaterials. Porous silicon (pSi), a generally biodegradable and biocompatible material that can be fabricated to include environment-responsive optical characteristics, is an excellent candidate for *in vivo* biosensors. However, the feasibility of using this material as a subcutaneously implanted optical biosensor has never been demonstrated. Here, we investigated the stability and biocompatibility of a thermally-hydrocarbonised (THC) pSi optical rugate filter, and demonstrated its optical functionality *in vitro* and *in vivo*. We first compared pSi films with different surface chemistries and despite the outstanding stability of the THC pSi films, the material was found to be cytotoxic. We then showed that the cytotoxicity correlates with reactive oxygen species levels, which could be mitigated by pre-incubation of THC pSi (PITHC pSi). PITHC pSi facilitates normal cellular phenotypes and is biocompatible *in vivo*. Importantly, the material also possesses optical properties capable of responding to microenvironmental changes that are readable non-invasively in cell culture and subcutaneous settings. Collectively, we demonstrate, for the first time, that PITHC pSi rugate filters are both biocompatible and optically functional for lab-on-a-chip and subcutaneous biosensing scenarios. We believe that this study will deepen our understanding on cell–pSi interactions and foster the development of implantable biosensors.

Keywords: Silicon, Cytotoxicity, Biocompatibility, Biosensor, Biodegradation, Subcutaneous implant

1 Introduction

Porous silicon (pSi) is regarded as an exciting biomaterial that frequently meets the high-level demands posed by a broad range of endeavours in future and nanomedicine. This class of materials can be economically and easily manufactured through anodic etching of silicon wafers in solutions of hydrofluoric acid. Through the control of the etching parameters, pore geometry of the pSi layer can be conveniently altered to meet the criteria of various medical applications and surface chemistry can be modified via a range of reactions including silanisation, hydrosilylation and hydrocarbonisation [1]. Such pSi structures are biodegradable in a physiological environment *via* oxidative hydrolysis in water [2], and the degradation product, silicic acid, is non-toxic [3]. pSi is ostensibly biocompatible *in vitro* and *in vivo* [4, 5], although freshly etched pSi particles have shown to cause cell death *via* generation of reactive oxygen species (ROS) [6] and Shabazi *et al.* have demonstrated a surface chemistry and cell type dependent cytotoxicity of pSi nanoparticles towards immune cells [7]. Another useful attribute of pSi is its set of optical capabilities that include photonic and photoluminescence effects, both being tunable across the visible spectrum. Because of these salient features, pSi is being pursued as a tissue scaffolding material [8], as a drug delivery vehicle [9] and, in nanoparticle form, as a bioimaging agent [10].

The construction of optical biosensors, based on the white light reflectance spectra produced by pSi, is another area of intense research activity in the biomedical field [11]. To produce such optical sensors, nanostructured forms of pSi are precisely prepared to form either an optical rugate filter, which reflects light only at specific wavelength, or a microcavity, which absorb light only at certain wavelength [12]. Such biosensors work on the fact that the wavelengths of the reflected/ absorbed light change according to refractive index changes inside the pores [13]. With such special optical characteristic, it has been proposed that a smart drug release carrier that self-reports the rate of release could be developed to meet clinical needs [14]. Recently, the development of implantable biosensors that passively and non-invasively report physiological changes, could possibly be engendered based on pSi [15, 16]. Such an implantable biosensor will have profound impact on the realisation of *in situ*, long distance diagnostics, and will revolutionise future medicine. However, for an implantable optical biosensor based on pSi, the hydrolytic instability of pSi under physiological conditions, uncertain biocompatibility, and the measurement of optical signal through the tissue are the significant challenges [17].

Several approaches have been explored to stabilise pSi structures and the improved stability by hydrosilylation [18] and thermal oxidation [19] has been exploited for drug-release, biosensing and lab-on-a-chip (LOC) diagnostic settings [20-23]. However, even greater stability is required for long-term, sustained, self-reporting drug-release and biosensing applications. In recent times, thermal hydrocarbonisation (THC) has become a method of choice for surface-treating pSi particles in order to produce materials that are stable for weeks under physiological conditions, but eventually degrade [24, 25]. However, only limited information on the biocompatibility of this THC-functionalised material is available. The majority of the existing investigations focus on the particulate form of pSi, fabricated from wafers with a specific doping level (or resistivity), which are not often used to prepare optical biosensors [26, 27]. To the best of our knowledge, there is no evidence demonstrating the optical functionality of implanted pSi films, and the reading of the optical signal from such implant has never been demonstrated in detail.

To bridge this knowledge gap, we aimed to first investigate in detail the cell and tissue responses to THC modified pSi (THC pSi) surfaces, in terms of stability and biocompatibility. We focused our investigation on pSi rugate filters made from highly doped p-type silicon wafers, since this format of pSi is very popular for self-reporting drug delivery [14, 28], and biosensors [11, 29]. At first, we investigated the degradation of THC pSi surface in cell culture medium and the effect on the optical properties in comparison to a conventional thermally oxidised pSi surface. We then studied the *in vitro* biocompatibility of these surfaces and were surprised to observe substantial cytotoxicity from THC pSi and certain thermally oxidised forms of pSi. This result triggered an investigation into the cause of the observed cytotoxicity and into possible mitigation strategies. Our results showed that pre-incubation of THC pSi (PITHC pSi) fully eliminated cytotoxicity. We then compared the *in vivo* tissue responses to THC pSi, PITHC pSi and polycaprolactone (PCL) with a murine surgical model, in order to demonstrate the biocompatibility of the pSi we developed. We further demonstrate that such biocompatible PITHC pSi rugate filter is optically functional and is measurable non-invasively in both cell culture and subcutaneous settings. We envisage that the knowledge presented here is a crucial step towards the development of the next generation of pSi-based biomedical devices. As the lifetime/stability and biocompatibility of these structures are enhanced, the development of advanced LOC, self-reporting drug delivery and *in vivo* passive biosensing applications are well within sight.

2 Materials and Methods

2.1 Fabrication of pSi rugate filters

pSi rugate filters were produced from p-type, boron doped, 1 mΩcm silicon, (Siltronix, France). To prepare good quality optical structures, a sacrificial etch was performed to remove the parasitic layer of the silicon wafer [30, 31]. The silicon was etched at 50 $mAcm^{-2}$ for 30 sec in 3:1 $HF_{48\%(aq)}$:EtOH. The HF was removed and the porous surface was dissolved in 0.5 M $NaOH_{(aq)}$ before being washed with MilliQ H_2O, EtOH and acetone and dried under $N_{2(g)}$. The rugate filter was fabricated by anodic etching in 3:1 $HF_{48\%(aq)}$:EtOH, with a sinusoidal current waveform, cycled from 20 – 50 $mAcm^{-2}$, with a period of 7.5 or 8.5 s. The wafer was etched for 50 cycles, after which the HF was removed and the surface was rinsed with EtOH and acetone and dried under $N_{2(g)}$. For the preparation of free-standing pSi membranes, a lift off etch was performed using 60 $mAcm^{-2}$ for 30 sec in 1:2 $HF_{48\%(aq)}$:EtOH. The HF was removed and the membrane washed carefully with EtOH (3 ×) and allowed to air dry without disturbance. The prepared pSi rugate filters were functionalised immediately following etching.

2.2 Surface modification of pSi rugate filters

Thermal oxidation (TO) of pSi was performed in air using a tube furnace at temperatures of 500, 600 and 800 °C, each for a time of 1 h. The resulting samples were termed TO500, TO600 and TO800, respectively Thermal hydrocarbonisation (THC) was performed (following a previous reported procedure [24]) by placing the freshly etched pSi surface into a quartz tube and purging with $N_{2(g)}$ for 45 min at a rate of 3 L/min. After this time, acetylene gas was introduced together with $N_{2(g)}$ at a concentration ratio of 1:1 for a time of 15 min. The quartz tube was then placed into a

tube furnace pre-heated at 500 °C for 15 min. 30 sec prior to the end of heating, the acetylene flow was stopped and the quartz tube was removed from the furnace. The tube was allowed to cool to room temperature under $N_{2(g)}$ before the surfaces were removed.

2.3 Characterisation of rugate filters after surface modifications

Scanning electron microscopy (SEM): pSi rugate filter surfaces were observed using a Crossbeam 540 SEM (Zeiss, Germany). pSi surfaces were fractured in half to reveal the cross section of the pore structure and were mounted and coated with a 5 nm thick layer of platinum. Pore geometry and dimensions were characterised using ImageJ (v 1.44p). For surgically implanted pSi rugate filters, cross-sections were revealed naturally by normal microtoming of tissues. The rugate filter membrane, together with surrounding tissues were dehydrated and dried in hexamethyldisilazane (HMDS, Sigma Aldrich, H4875) against a filter paper and carbon-coated. For platinum-coated pSi surfaces, an accelerating voltage of 5 kV and an 'in-lens' detector at 2 mm working distance was used. For pSi embedded tissue sections mounted on glass slides, an accelerating voltage of 1 kV and an 'in-lens' detector at 2 mm working distance was used.

Infrared (IR) microscopy: Chemically modified pSi surfaces were characterised by IR microscopy using a Hyperion 1000 FTIR Microscope (Bruker, Germany). An ATR accessory with a germanium crystal and a liquid nitrogen cooled MCT detector was used to capture the spectra. All spectra were collected as an average of 64 scans, with a resolution of 4 cm^{-1}, over the range of 650 – 4000 cm^{-1}. A background of air was used to correct the raw spectra. Spectra were analysed using Opus software (Bruker).

2.4 Reflectance spectroscopy

Optical reflectance of the pSi rugate filters *in vitro* and *in vivo* was characterised by reflectance spectroscopy. White light from a tungsten lamp was focused on the surface through a bifurcated fibre optic probe and reflected light (collected using the same probe) was directed to an Ocean Optics USB2000 spectrometer. Spectra were analysed using Spectra Suite software (v6.1, Ocean Optics 2008).

For the *in vivo* optical reflectance, mice subcutaneously implanted with pSi rugate filter were anesthetised under isoflurane. The fibre optic probe was then aligned and focused on the implant surface. The handheld fibre optic probe was then aligned and focused on the implant surface maintaining a 90° incidence angle during measurement. Deviation from 90° incident angle reduces only the intensity of the measured spectrum and does not affect the position of the rugate peak due to the use of the bifurcated fibre optic probe. Spectra were recorded using the reflection of a blank region of mouse skin as blank. This procedure was approved by the SA Pathology Animal Ethics Committee (Approval number, SAM#72).

2.5 ICP-MS measurements

An Agilent triple quadrupole ICP-MS (ICP-QQQ - 8800, Tokyo, Japan) was used for silicon (Si) and boron (B) detection. Measurements were carried out in two gas modes (Helium; He and Oxygen; O_2) to reduce spectral interferences. The instrument was

tuned on a daily basis for maximum sensitivity (an oxide ratio of < 1.0% ($^{140}Ce^{16}O^{+}/^{140}Ce^{+}$) and a double charged ratio of < 1.5% ($^{140}Ce^{2+}/^{140}Ce^{+}$) with background counts of < 0.1 cps. The mass-shift (MS/MS) mode with O_2 gas cell (0.40 ml min^{-1}) was used to measure Si as SiO^{+} at m/z 44 (Q1 = 28 and Q2 = 44). Boron was measured in single quadrupole (m/z = 11) using He gas mode (5.0 ml min^{-1}). All acids used were either Analytical Reagent (AR) or Trace Analysis Grade (TAG) from Fisher Scientific, UK and ≥ 18.2 MΩcm Milli-Q water was used throughout. Internal standards introduced to the sample stream via ISIS discrete sampling using T-piece included Sc and Ir (100 µg l^{-1}) in 2 % v/v TAG HNO_3. Stock single element solutions containing 1000 mg l^{-1} of Si and B (High-Purity Standards, Australia) were used to prepare the external calibration standard solution by diluting in 2 % v/v TAG HNO_3. The same standards were used for preparation of the continuing calibration verification (CCV) standards for quality control purposes (general % recoveries were 98.4 % Si and 99.5 % B).

2.6 Cell culture

Fibroblasts are one of the major cell types in connective tissues for laying down extracellular matrix and are involved in the wound healing process. Therefore, a fibroblast cell line (NIH3T3, mouse embryonic, ATCC CRL-1658) was chosen in our *in vitro* studies. Cells were maintained in Dulbecco's modified eagle medium (DMEM) high glucose (Sigma, D5671) with 10 % fetal calf serum and 1 % antibiotic – antimycotic (Invitrogen, 15240-062) at 37 °C and 5 % CO_2 in a humidified incubator. The media was refreshed every three days. Cells thawed from stock were passaged at least twice, and all cultures were maintained at less than 90 % confluence before performing experiments on pSi samples.

2.7 Cytotoxicity assessments

Differently treated pSi rugate filters were incubated in DMEM at 37 °C and 5 % CO_2 in a humidified incubator. Every two days DMEM containing degradation products from each samples were collected, and samples are incubated in fresh DMEM. This was repeated until day 14 (Figure 2A). In parallel, cells were seeded onto tissue culture wells at a density of 1×10^4 cells cm^{-2}. After 3 h, normal DMEM was removed, and replaced by the DMEM containing degradation products from pSi rugate filters. After 24 h of culture, cells were imaged under a phase contrast microscope. Based on these images, the number of necrotic and non-necrotic cells in each group were identified and counted based on the morphological criteria described by Rello *et al*. [32]. The average fraction of these cells in the whole population was reported as the "proportion of non-necrotic cells (%)". Higher percentage directly reflects the higher cytocompatibility.

For cytotoxicity assessment of cells exposed to different concentrations of H_2O_2 as a positive control, cells were also seeded at a density of 1×10^4 cells cm^{-2} in tissue culture wells, followed by exposure to 0 -1250 µM of H_2O_2. For consistency, cytotoxicity was assessed by the morphological criteria mentioned above, and the proportion of non-necrotic cells (%) reported.

2.8 Quantification of reactive oxygen species (ROS) by the DCFH assay

The ROS generation difference between differently treated pSi rugate surfaces was investigated by the dichloro-dihydro-fluorescein (DCFH) assay. TO800 and THC treated pSi rugates were first incubated in DMEM for 2 days. After incubation, DMEM was collected for immediate analysis. A serial dilution of H_2O_2 in DMEM was prepared to serve as standards. The assay followed the protocol described by Pal *et al.* [33]. Briefly, DCFH diacetate (Sigma, D6883) was first dissolved into ethanol to make a stock solution of 1 mM. Assay buffer was made fresh by diluting the stock solution 1 : 4 into 10 mM NaOH to hydrolyse the ester. After 30 min, the solution was neutralised in PBS to make up a DCFH concentration of 10 μM. Assay buffer was mixed with samples and standards at a ratio of 1:9 (sample:assay buffer). In this cell-free assay system, peroxidase (Sigma, P6782) was supplemented to the mix at a final concentration of 0.04 U to aid the oxidation of DCFH [34]. After 10 min incubation, all samples were then analysed on a fluorescence plate reader (LS 55 FluorescenceSpectrometer, PerkinElmer). For the ROS value obtained to be biologically meaningful, fluorescence values were converted to H_2O_2 equivalents [35, 36].

2.9 Immunofluorescence imaging of cell morphology and fibrotic layer formation

THC-pSi rugate filter surface was pre-incubated in medium for 10 days at 37 °C, the surfaces, namely PITHC pSi, were then rinsed with PBS twice before cell culture.

To investigate cell spreading *in vitro*, cells were seeded at a density of 1×10^4 cells cm^{-2} onto PITHC pSi, as well as on TCPS and pre-incubated THC flat silicon wafers as controls. After 24 h, cells were fixed for 5 min with 4 % freshly prepared PFA at room temperature and washed twice with PBS before permeablisation in 1 % Triton X-100 in PBS for 2 min at room temperature. After permeablisation, the cells were washed twice in PBS and blocked with 1 % bovine serum albumin (BSA) in PBS for 30 min at room temperature. Cell nuclei and actin filaments were then labeled with Hoechst 33342 (Invitrogen, H1399) and phalloidin-rhodamine (Sigma, P1951), respectively, for 30 min.

The ECM deposition and tissue formation on THC rugate filter was induced by a procedure based on Chen *et al*. [37] and Paul *et al.*[38] to induce ECM deposition of fibroblast. Briefly, cells were seeded onto PITHC pSi at a higher density of 5×10^4 cells cm^{-2}. After 24 h, medium was refreshed and supplemented with 5 ng/ml of TGF-β1 (Chemicon, GF111) and 100 μM of ascorbic acid (Fluka, 49752). Medium was refreshed twice a week, for a total period of two weeks. To image the formed fibrotic matrix, cells were fixed, permeabilised, and blocked with BSA. Cells were then incubated with primary antibody against collagen 1 (Santa Cruz, sc-25974) for 1 h, followed by 1 h incubation with secondary antibody Alexa 488 donkey anti-goat IgG (Invitrogen, A11055). Cell nuclei and actin filaments were then counterstained with Hoechst 33342 and phalloidin- rhodamine, respectively.

After washing, cells on surfaces were mounted against a coverslip with fluorescence mounting medium (IM030, ProSciTech). These samples were then imaged using a confocal microscope (Nikon A1-R).

2.10 Cell proliferation

The proliferation rate of fibroblasts spreading on TCPS, PITHC silicon and PITHC pSi was assessed through pulse labeling of cells using the Click-iT EdU imaging kit (Invitrogen, C10337). Briefly, cells were seeded on the three substrates at a density of 2×10^5 cells cm^{-2}. After 24 h, cells were incubated with 10 µM of EdU (5-ethynyl-2-deoxyuridine) in DMEM. Cells on substrates were then fixed in 4 % PFA and permeablised in 0.5 % Triton X-100 in PBS. S-phase cells, which are EdU positive, were visualised following the protocol specified by manufacturer. All cells were counter-stained by Hoechst 33342. Cells labeled as EdU positive and the total cell number were counted. The averaged ratio of S phase cells to the total number of cells is reported as "proportion of S phase cells". This directly reflects the proliferation rate of cells.

2.11 Surgical insertion, tissue harvesting and processing

After identifying the most stable and cytocompatible pSi rugate filters by *in vitro* studies, the biocompatibility was further evaluated in a mouse model in terms of tissue responses. The mouse strain skh:hr, was chosen for their hairless characteristics and intact immune system, such that the implant could be easily located and immune responses could be characterised without interference. All procedures described in this study were approved by the SA Pathology Animal Ethics Committee (Approval number, SAM#72).

Mice at 10-14 weeks of age were obtained from Prof. Reeve (University of Sydney) and acclimatised in a rodent room for at least 1 week prior to any procedures. Unlimited food and water was provided ad libitum. A total of 6 mice were allocated for the experiment, they were randomly divided into three groups. PITHC and THC pSi (THC) were prepared as described above. Polycaprolactone (Sigma, Z724416), a FDA approved implant material was used as a control. All implants were prepared as films with a size of approximately 5 mm x 5 mm x 2 mm. Surgical procedures were conducted under anesthesia (isoflurane), on a heat-pad for maintaining body temperature. Subcutaneous pockets were opened by using blunt forceps. Then, each group of mice was surgically implanted with one of the implants in their dorsal right subcutis. No implant (sham) was on their left dorsal subcutis. Open wounds were closed by using a 5-0 monofilament absorbable suture (Syneture Caprosyn, SC-5626G). These mice were monitored, and surgical wounds were checked every day. All mice were humanly killed by cervical dislocation under anesthesia at 1 week post-surgery. Skin, liver and spleen tissues were harvested and rinsed in saline, followed by immersion-fixation in neutral buffered formalin (NBF, Chemsupply) at 4 °C for 3 days. After fixation, NBF was removed under running tap water, and tissues were dehydrated in serial increment of ethanol concentrations. Dehydrated tissues were infiltrated and embedded in paraffin with the aid of a tissue processor (Thermo Scientific Excelsior). Resulting tissue blocks were stored ambient for sectioning.

2.12 Tissue staining

Tissue sections obtained by microtoming were incubated at 50 °C overnight, followed by deparaffinisation and rehydration. To examine overall tissue structure, skin, liver and spleen tissues sections were staining by hematoxylin and eosin (H&E). Lillie-mayer's H&E (Australian Biostain P/L) was used, and staining was conducted following standard protocols. To visualise the collagen contents in proximal skin

tissues, rehydrated slides were incubated with Picro-sirius red solution (Abcam, ab150681) for 60 min. Slides were then rinsed in 0.5 % acetic acid, and ethanol. Stained slides were dehydrated and mounted against coverslips in water-free xylene based mountant DPX (Sigma, 06522).

To investigate inflammatory response, skin sections were probed against pro-inflammatory cytokines interleukin-6 (IL-6). Rehydrated slides were incubated in sodium citrate buffer pH 6 at 95 °C for 30 min for antigen retrieval. Slides were incubated in 1 % H_2O_2 for 15 min to quench endogenous peroxidase activity, followed by serum blocking. Slides were then incubated with goat anti-mouse IgG Fab (Abcam, ab6668) for 1 h to block endogenous IgG. After washing, slides were incubated with primary against IL-6 (Santa Cruz, sc-1265-R) overnight at 4 °C. Slides were then incubated with biotinated mouse-rabbit polyvalent secondary (Abcam, ab64264), followed by strepavdin peroxidase (Abcam, ab64264) incubation. After washing, slides were developed using 3,3'-diaminobenzidine (DAB) substrate for 15 min. Slides were counterstained by Lillie-Mayer's haematoxylin, and eventually coverslipped in DPX.

H&E and immunohistological stained tissue sections were imaged using a bright-field microscope. Picro-sirius Red stained slides were imaged under a microscope equipped with a polarisation filter.

2.13 Statistics

Experiments are reported in triplicates unless otherwise stated. Error bars presented in charts equal ± 1 standard deviation (SD). Statistical differences were tested by non-parametric Mann-Whitney U-test. The hypothesis was accepted at a 95 % significant level ($p < .05$).

3 Results

3.1 Chemical, structural, and optical characterisation of pSi rugate filters modified by different surface treatments

In this study, we first sought to identify surface treatments that yield stable pSi rugate filters fit for purpose in implantable biosensor applications, and then we studied the cytocompatibility of these modified pSi surfaces. We then focused on one of the surfaces that was stable as well as cytocompatible, and characterised this in detail in terms of the cell and tissue response.

The cross-sectional structure of the THC pSi rugate filters was investigated by means of SEM. A layered pore structure consistent with the pSi rugate filter design was seen at low magnification (Figure 1B). A higher magnification image shows that the pore dimension of the THC pSi rugate filters are between 5 nm and 15 nm for the low and high porosity layers, respectively (Figure 1C). An as etched pSi rugate filter displayed the same pore size as for the THC treated surface, while a 500 °C thermally oxidised surface showed reduced pore sizes (< 8 nm) due to the oxide layer reducing the pore diameter [39]. The optical reflection spectrum measured demonstrates a photonic peak of the rugate filter at 560 nm (Figure 1D).

Thermal oxidation (TO) and thermal hydrocarbonisation (THC) are surface treatments for pSi that are known to delay the hydrolytic degradation of pSi materials [24, 40, 41]. We modified highly doped (p^{++}) pSi rugate filters by TO at 500 °C, 600 °C and 800 °C (denoted as TO500, TO600 and TO800 pSi, respectively), and by THC (THC pSi). These surfaces were analysed by IR spectroscopy. The IR spectrum of the freshly etched pSi rugate filter shows Si-H absorption bands at 2100 cm^{-1} and 900 cm^{-1} [42], while TO pSi and THC pSi rugate filters show Si-O and Si-C absorption bands at 1030 cm^{-1} and 1010 cm^{-1} [25, 43], respectively. The TO pSi surface also shows an adsorption band at 800 cm^{-1} corresponding to Si-O-Si vibrations, while the THC surface shows an absorbance at 790 cm^{-1} corresponding to Si-C vibrations [44]. The THC pSi rugate filter also shows weak absorption bands at 2920 cm^{-1} [45], corresponding to C-H stretching vibrations (Figure 1E). These spectra indicate the successful completion of surface modifications. These characterisations collectively indicate that desired rugate microstructure with various chemical functionalities were obtained.

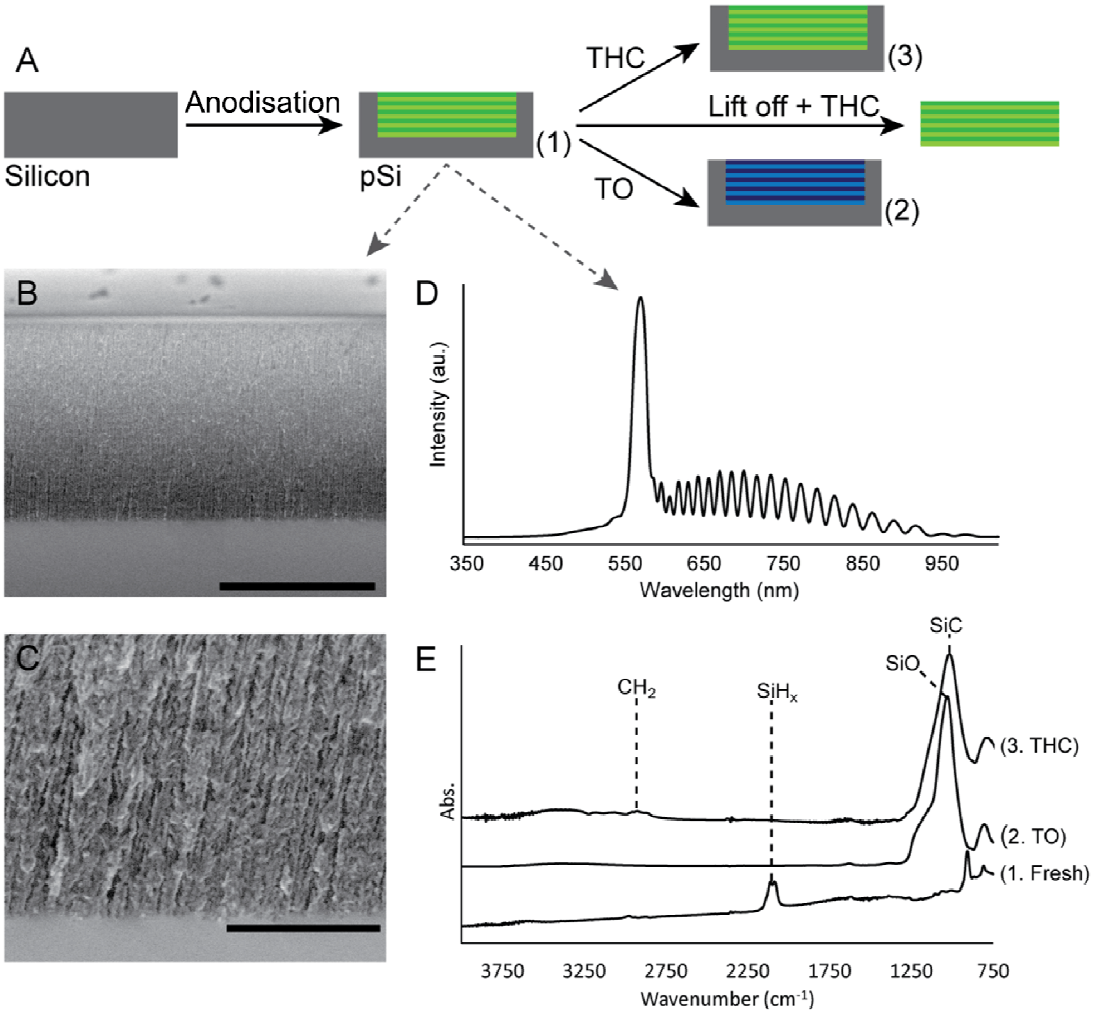

Figure 1: Preparation and characterisation of pSi rugate filters. (A) Schematics of the manufacturing of pSi films and membranes. (B&C) SEM of cross-section of pSi. Scale bars represent 3 µm and 400 nm, respectively. (D) Reflection spectrum of pSi rugate filter. (E) IR spectra of (1) freshly etched, (2) TO and (3) THC pSi.

3.2 The stability of surface-modified pSi rugate filters

After the characterisation of the surface treatments, we investigated the effect of those treatments on the stability of the pSi structures in cell culture medium (DMEM) at pH 7.4 and 37 ˚C, to mimic a physiological environment. The stability of TO500, TO600, TO800 and THC surface modifications was assessed by monitoring the Si concentration in the DMEM using ICP-MS. The DMEM was replaced every 2 days for 12 days (Figure 2A). DMEM carrying the degradation products of TO500 pSi, TO600 pSi, TO800 pSi and THC pSi are termed TO500 pSi/DMEM, TO600 pSi/DMEM, TO800 pSi/DMEM, THC pSi/DMEM, respectively. ICP-MS result shows that TO500 pSi, TO600 pSi and TO800 pSi ceased to release Si and B ion into DMEM starting from day 4, 6 and 8, respectively (Figure 2B). This indicates that TO500 pSi had dissolved almost completely after day 4, whereas TO600 pSi dissolved over 6 days and TO800 pSi over 8 days. Only THC pSi stably released Si and B over the course of 14 days, indicating that the porous structure was relatively stable over the entire timeframe of the experiment (Figure 2B). Material degradation coincided with a loss of the optical properties of the material, with the exception of THC pSi (Figure 2C). This is evident from the significant blue shift of the TO500 rugate peak between day 2 and 4 and then subsequent loss of its optical properties thereafter. The TO600 surface also lost its optical properties following the measurement at day 2. This is in contrast to the THC pSi surface that maintained its optical properties for the entire time course of the experiment. The THC pSi surface showed a small blue shift between day 4 and 8 and a more pronounced shift between day 8 and 12. However, the optical properties were still maintained after this time. In comparison, a freshly etched pSi surface was fully degraded within a two day time period. For the THC pSi, whilst there was slow release of Si and B, the photonic resonance was maintained over 16 days. Note that the TO800 pSi did not produce a photonic resonance due to the loss of refractive index contrast upon oxidation (Figure 2C) [46, 47].

Therefore our results show that the THC surface modification of the pSi yields the most stable surface under physiologically relevant working conditions and retains the photonic properties of the rugate filter over the long period of time, which is important for an implantable biosensor.

ACCEPTED MANUSCRIPT

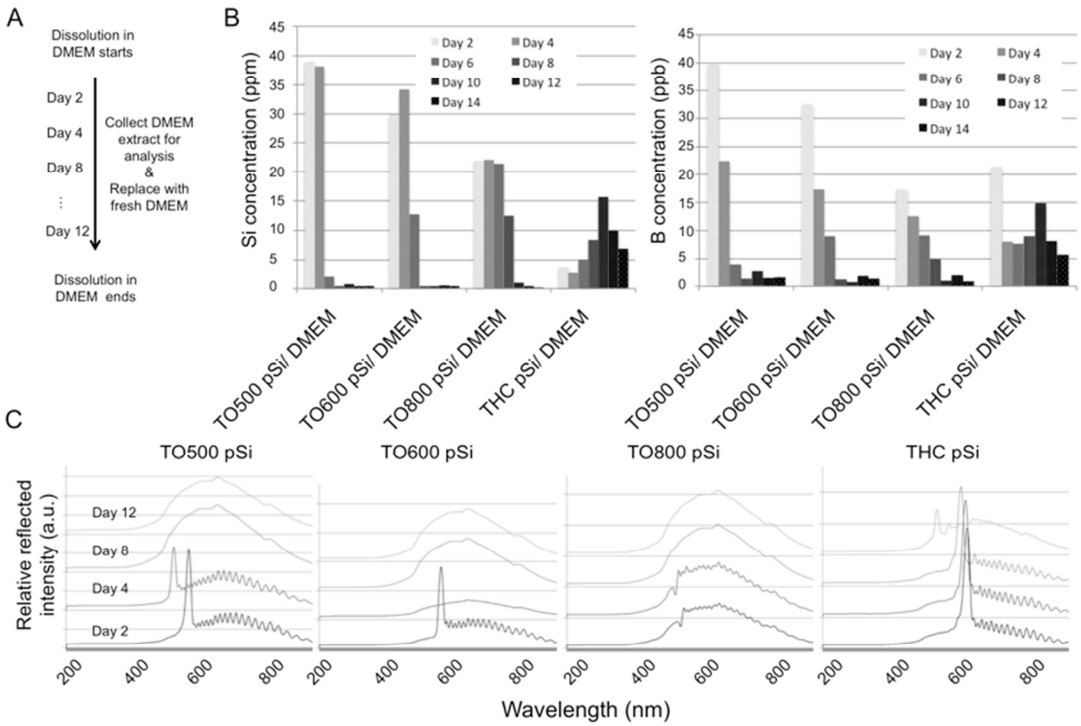

Figure 2: Stability of surface-modified pSi rugate filters in physiological conditions. (A) Illustration of the time-points for collection of degradation products from pSi. (B) Effect of surface treatments on Si and B release as determined by means of ICP-MS. (C) Effect of surface treatments on reflection spectra.

3.3 The effect of pSi rugate filter surface treatment on cytotoxicity

The excellent stability of THC pSi rugate filters in physiological conditions prompted us to investigate their biocompatibility. Biocompatibility of degradation products from TO500, TO600, TO800 and THC pSi samples were first investigated *in vitro*. These pSi rugate filters were first incubated with DMEM. These media were collected every two days, and are referred to as TO500 pSi/DMEM, TO600 pSi/DMEM, TO800 pSi/DMEM and THC pSi/DMEM, respectively. Fibroblasts cultured on a standard well plate were then exposed to respective degradation products by incubating in the collected DMEM. Figure 3A shows the morphology of fibroblasts exposed to these DMEM at 24 h post-exposure. We observed that cells exposed to TO500 pSi/DMEM, TO600 pSi/DMEM and THC pSi/DMEM (media collected after 2 days incubation) displayed a rounded morphology and detached from the culture surface, with their cell bodies consumed by a single big evagination (Figure 3A inset, white arrows). These resemble typical acute necrotic cell morphology, indicating necrotic cell death. This cross-validates FDA/PI staining of fibroblast culture on TO500 pSi and THC pSi surfaces that shows rounded cell bodies with compromised cell membrane (Figure S1A). Based on the morphological criteria, we differentiated between necrotic and viable cells [32] and obtained the percentage of non-necrotic cells to directly reflect the cytocompatibility of pSi degradation products. This quantitation revealed that TO500 pSi/DMEM and TO600 pSi/DMEM on day 2 and day 4 had a high percentage of necrotic cells, indicating respective degradation products were cytotoxic. Such cytotoxicity started to subside for media collected at day 6 (Figure 3B). We attribute these results to the complete degradation of TO500

and TO600 rugate filter surfaces after day 6 (Figure 2B). For THC pSi rugate filter, whilst almost 100 % of the cells were necrotic when exposed to THC pSi/DMEM collected on days 2, 4 and 6, the percentage of non-necrotic cells was substantially increased in medium collected after day 10. This result indicates that the THC pSi becomes cytocompatible after 10 days of incubation (Figure 3B, black arrow). In contrast, DMEM extracts from TO800 pSi were shown to be cytocompatible throughout the entire experiment (Figure 3B). Since degradation product released from THC pSi rugate filter, which has been incubated for 10 days, is cytocompatible to fibroblasts, and this rugate filter also retained its photonic properties (Figure 2C), we envisage that pre-incubating treatment of THC pSi rugate filter would be a suitable approach to mitigate cytotoxicity. Therefore, we termed the pre-incubated THC rugate filter as PITHC, and included it in further experiments.

The observed cytotoxicity of the degradation products from TO and THC treated rugate filters prompted us to investigate its origin. Firstly, we studied the effect of different dopants on cytotoxicity. For highly doped n-type silicon (n^{++}), we observed similar results to p^{++} pSi. Namely, the TO800 modification was cytocompatible, but TO600 and THC pSi (n^{++}) were cytotoxic in indirect contact (Figure S1B). This indicates that dopant itself may not be the cause of the cytotoxicity. In contrast, higher resistivity p-type pSi samples were not cytotoxic (Figure S1C), suggesting that the cytotoxicity of degradation product may be related to the doping level. Secondly, we next investigated the toxicity of the degradation product of a rugate filter before surface treatment (As-etched pSi/DMEM). Keeping in mind the fact that an as-etched pSi rugate filter completely degrades within 24 h in physiological solutions, as-etched pSi was only immersed in DMEM for 18 h. Figure S2A shows the morphology of fibroblast after exposure to as-etched pSi/DMEM for 1 day. Necrotic cells were observable (60 %) indicating that as-etched/ DMEM also inducted certain level of cytotoxicity. However the population of non-necrotic cells is obviously higher than the cells exposed to TO500 pSi/DMEM, TO600 pSi/DMEM and THC pSi/DMEM, indicating that as-etched pSi/ DMEM is less cytotoxic.

Since substantial amounts of Si and B were found in medium incubated with TO and THC pSi, we also investigated their role in the cytotoxicity observed, by correlating the concentration of Si and of B dissolved in DMEM (determined by means of ICP-MS) with the percentage of non-necrotic cells. This is illustrated in Figure S2B and S2C. We found no obvious correlation. In particular, the level of Si in the degradation product of TO800 pSi (day 2-6) was higher than the Si found in the in THC pSi degradation product at any time point. However, TO800 pSi degradation products were found to be cytocompatible but not THC pSi degradation products (Figure S2B, asterisk). Similarly, although the B concentration in the degradation product of TO800 pSi at day 2 is higher than that of THC pSi at day 4 and 6, TO800 pSi is found to be cytocompatible but not THC pSi (Figure S2C, hash). These results show that although a considerable amount of Si and B was released into the cell culture medium, the observed cytotoxicity was not a direct result of dissolved Si and B.

Given that the released Si or B were not responsible for the observed cytotoxicity, we suspected that the toxicity might be due to reactive oxygen species (ROS) formation [6]. TO500 pSi and TO600 pSi were not hydrolytically stable enough to maintain photonic properties and were hence excluded from the following study. Instead, we compared TO800 pSi, and PITHC pSi with THC pSi in terms of ROS formation using

the DCFH assay. Our results indicate that the ROS level in DMEM from THC pSi is significantly higher than that of TO800 pSi and PITHC pSi by at least 4 fold (Figure 3C). The ROS level therefore does correlate with the cytotoxicity, which indicated THC pSi/ DMEM was cytotoxic, but TO800 pSi/DMEM and PITHC pSi/DMEM were not. The oxidation power of the THC pSi/ DMEM is estimated to be equivalent to the oxidation power of 360 μM of H_2O_2 (Figure 3C). Such oxidation level causes a substantial level of cell necrosis (Figure S2D); this indicates that ROS generated by the THC pSi rugate filter surfaces contribute to the cytotoxicity observed.

Previous studies show that oxidation of pSi microparticles reduces their ROS generation [6]. In agreement with this report, we observed that ROS levels in as-etched pSi/DMEM was higher than that of TO800 pSi/DMEM, while lower than that of THC pSi/DMEM (Figure S2E). This coincides with the cytotoxicity result, suggesting as-etched pSi/DMEM is less cytotoxic than THC pSi/DMEM.

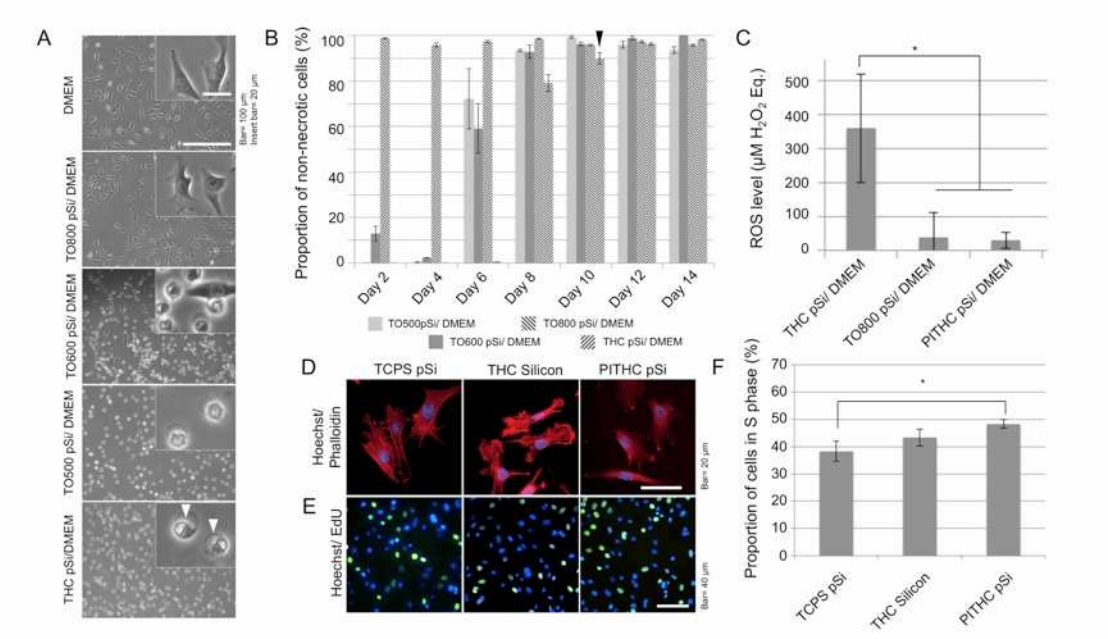

Figure 3: Cytotoxicity, cell morphology and proliferation on surface-modified pSi rugate filters. (A) Phase-contrast microscopy of NIH3T3 morphology after 24 h exposure to DMEM extracts from day 2 incubation with pSi rugate filters. Insets show magnified representative morphology. (B) Cytotoxicity of degradation products from surface-modified pSi rugate filters collected at different time points reported in terms of the proportion of non-necrotic cells. (C) Comparison of ROS level between THC, TO800 and PITHC pSi rugate filters, reported as H_2O_2 equivalents (μM). (D) Cell morphology of NIH3T3 cultured on TCPS, THC silicon and PITHC pSi rugate filter surface at 24 h post-seeding. Actin filament in red, cell nuclei in blue. (E) EdU incorporation assay. Green: EdU labeled nuclei of cells in S phase. Blue: all nuclei. (F) Proliferation rate of fibroblasts cultured on TCPS, THC silicon, and PITHC pSi. *(*represents $p<.05$)*

3.4 PITHC pSi rugate filter possesses optical functionality while maintaining fibroblast phenotype

To further investigate the biocompatibility of the PITHC pSi rugate filters, fibroblast adhesion and spreading on this surface was compared to TCPS. A DMEM pre-incubated THC flat silicon was also included as a control to evaluate the influence of surface topography. There was no observable difference in the number of cells adhered on these three surfaces. Fibroblasts were found to have a similar ability to spread on the PITHC pSi surfaces as compared to TCPS (Figure 3D). More importantly, cell spreading area and the number of filopodia protrusions were virtually indistinguishable to TCPS and the THC flat silicon. Firstly, this demonstrated that the surface roughness in this case does not affect cell adhesion and spreading. Secondly, since filopodia protrusion is involved in the upstream of cell adhesion dependent survival signaling [48], this result suggests that PITHC pSi rugate filters are able to support adherent cell survival. Interestingly, it was also observed that stress fiber formation within the cells cultured on PITHC pSi rugate filters was less pronounced as compared to TCPS and THC silicon (Figure 3D). This may reflect the fundamental differences of the mechanical properties between porous and non-porous structures, which can result in differences in mechanotransduction [49].

To investigate possible phenotypical changes in fibroblasts adhering to PITHC pSi, the proliferation rate of fibroblasts on TCPS, THC silicon, and PITHC pSi were compared. Nuclei of cells entering S phase were pulse labeled with EdU (green) while all nuclei were labeled with Hoechst (blue) (Figure 3E). A higher proportion of cells entering the S phase indicates higher proliferation rate. We observed that the proliferation rate of cells on PITHC pSi was significantly higher than on TCPS, while there was no significant difference between cells on TCPS and THC silicon (Figure 3F). This result indicates that PITHC pSi surface does not impede the proliferation of fibroblasts.

A major role of fibroblasts is to deposit collagen fibrils as an extracellular matrix (ECM) during wound healing and maintaining tissue homeostasis [50]. It is therefore important to further investigate such phenotype for the fibroblasts cultured on PITHC pSi. We cultured fibroblasts on PITHC pSi rugate filters in confluence under the stimulation of TGFβ1 and ascorbic acid for 10 days. It was observed that fibroblasts were able to populate and proliferate to cover the surface of the PITHC pSi with and without stimulation (Figure 4A,B). However, fibroblasts cultured on PITHC pSi under stimulation were able to deposit substantially more collagen type 1 into the surrounding as compared to the non-stimulated fibroblast layer (Figure 4C). Stimulated fibroblasts formed multilayered fibrotic capsules on the PITHC pSi surface (Figure 4C). These observations collectively suggest that proliferation and secretion of ECM are not hindered on the PITHC pSi rugate filter surface.

Figure 4D shows the overall appearance of PITHC pSi rugate filters covered with the *in vitro* tissue layer formed by the fibroblasts. After 3 weeks of cell culture, the sample still maintained the appearance of a rugate filter, and the photonic peak measured by IRS demonstrated that the characteristic photonic properties could be probed through the fibrotic capsule (Figure 4E). The reflectance spectra before and after fibrotic capsule formation are displayed in Figure 4E. A small (~ 6 nm) blue shift in peak position is observed for the PITHC pSi rugate filter post fibrotic capsule formation. This may be attributed to minor surface degradation after 3 weeks in cell culture media and follows a similar trend to that displayed for the THC pSi surface in Figure 2C. A decrease in intensity of the rugate peak is also observed, which was

attributed to light scattering from the fibrotic capsule. We demonstrated sensing by exposing the induced-fibrotic layer covered PITHC rugate filter to solutions containing different concentrations of sucrose. The photonic peak red shifted to longer wavelengths in response to increasing sucrose concentrations (Figure 4F). The comparison of sucrose sensing on a PITHC rugate filter with and without the fibrotic capsule (Figure 4F) shows a near identical response to increasing sucrose concentration and confirms that the fibrotic capsule does not interfere with the sensing. This result demonstrates that, despite the PITHC rugate filter being covered with fibrotic tissue, the pores are still available to the infusion of analytes, and the subsequent change in peak position could be measured by IRS.

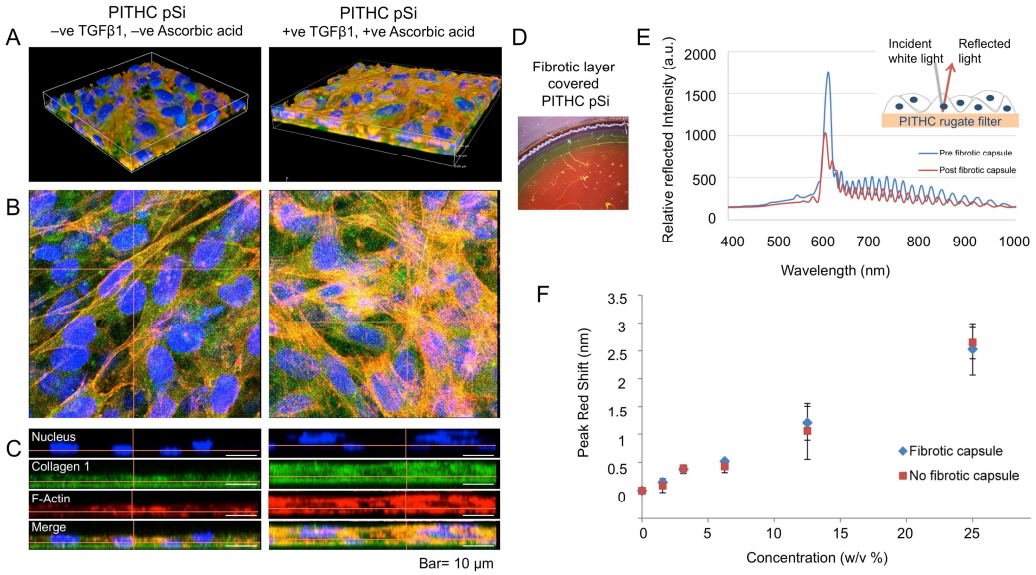

Figure 4: Fibrotic capsule formation by fibroblasts cultured on PITHC pSi rugate filter, and corresponding optical functionality. (A) 3D reconstruction of the confluent tissue layer formed by NIH3T3 on PITHC pSi with and without TGF-β1 and ascorbic acid stimulation. Collagen type 1 in green, actin filament in red, and nuclei in blue. (B) Top view and (C) cross-sectional views of NIH3T3 tissue layer on the PITHC pSi rugate filter. (D) Low magnification colour micrograph from stereomicroscope of PITHC pSi rugate filter populated with cells. (E) Reflectance spectrum of PITHC pSi covered with fibroblast-generated fibrotic capsule. (F) Photonic peak shift of PITHC pSi covered with fibrotic capsule in response to changes in sucrose concentrations.

3.5 Biocompatibility and optical functionality of subcutaneous PITHC pSi rugate filter implant

After demonstrating the cytocompatibility of PITHC pSi rugate filters *in vitro*, the biocompatibility of this material was further interrogated in a mouse model (Figure 5A). In order to illustrate the improvement of a PITHC pSi rugate filter, a THC pSi rugate filter was implanted as a comparator. Due to the fact that any implantation would induce foreign object response, the FDA approved implant material PCL was implanted in parallel as a further control. These implants were surgically inserted subcutaneously. Figure 5B shows a representative image of the surgical wound (THC pSi) at day 4 post-surgery, indicating that there was no swelling and that the surgical wound had closed.

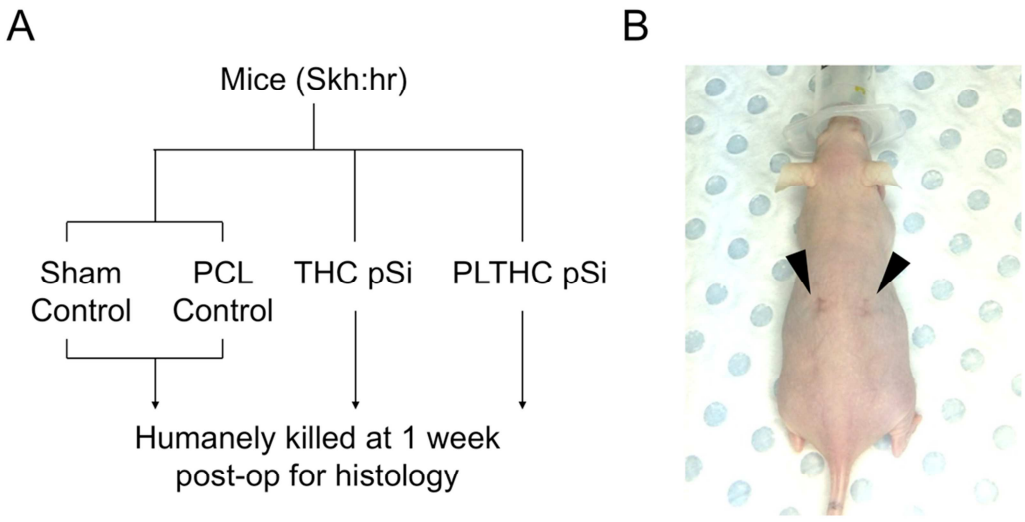

Figure 5: Schematic of *in vivo* study and the appearance of surgical insertion site. (A) Schematic of *in vivo* study. Experimental groups were either implanted with THC or PITHC pSi rugate filters membranes. PCL and Sham served as control. (B) Appearance of surgical wound around insertion site (arrows).

The subcutaneous tissues in close proximity to the implants were first examined by H&E staining. We observed signs of epidermal hyperplasia in both the PCL and THC pSi rugate filter group, but not in the Sham and PITHC pSi rugate filter (Figure 6A, arrows). This type of staining may indicate localised inflammatory processes [51]. This was confirmed by immunohistochemical (IHC) labeling of pro-inflammatory cytokine IL-6 in the epidermis (Figure 6B), which was co-localised with the hyperplasia region. H&E staining directly at the tissue-implant interface revealed necrotic, non-structural and loosened tissue around the THC pSi rugate filter, while the tissue architecture around the PCL and PITHC pSi rugate filter appeared to be structured with good tissue ongrowth onto the implant surface (Figure 6C, diamonds). In order to reveal the wound healing process around the implant, tissues around implants were staining with Picro-sirius Red and observed under a polarised microscope. There was strong green staining in the Sham, PCL and PITHC pSi groups, indicating an abundance of collagen type 3 (Figure 6D, white arrows). However, such staining was absent around the THC pSi rugate filter. As collagen type 3 is the major type of collagen present during wound healing [52], this difference may indicate that the normal healing process was hampered by the THC pSi rugate filter, but not in Sham, PCL and PITHC pSi rugate filter groups. IL-6 staining of the same area showed that there was a stronger inflammatory response around the THC pSi rugate filter as compared to the other groups, which in turn appeared all similar (Figure 6E). These observations collectively suggest that the PITHC pSi rugate filter shows a much better biocompatibility *in vivo* than the THC pSi, and that the tissue responses induced by the PITHC pSi rugate filter were not inferior to a PCL implant.

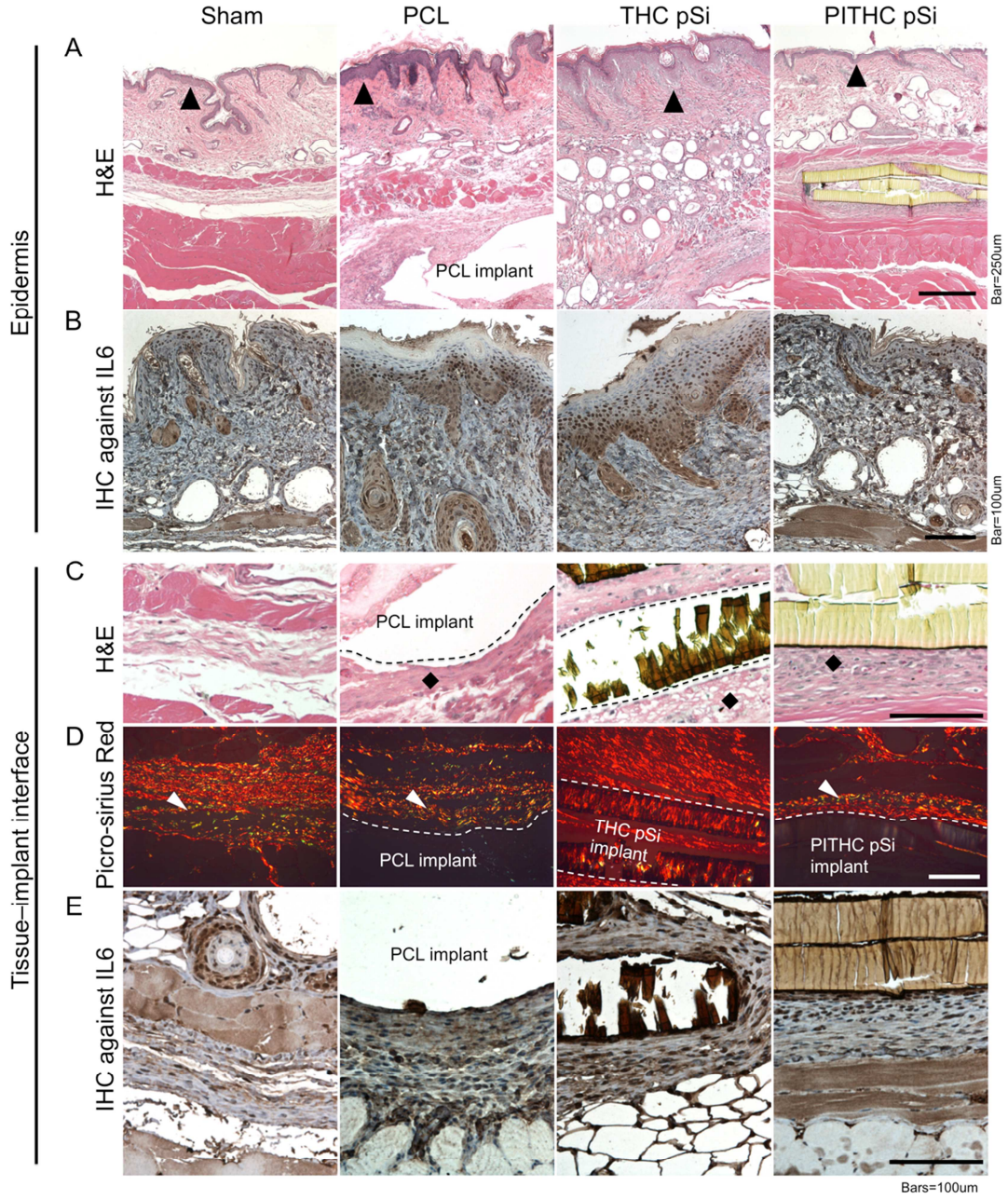

Figure 6: Histological comparisons of subcutaneous mouse tissue implanted with PCL, THC and PITHC pSi rugate filter membranes. (A) H&E staining of epidermal tissues located above PCL, THC pSi and PITHC pSi rugate filter membrane implants, respectively. Arrows indicate the edge of the epidermis. (B) IHC staining of IL-6 in epidermal tissues. (C) H&E, (D) Picro-sirius Red staining, and (E) IHC staining against IL-6 of at the tissue–implant interface. Diamonds indicate the implant-tissue contact. Picro-sirius Red stained tissues are imaged through a polarised filter. Here, red colour corresponds to collagen type 1 and green to collagen type 3 (labeled by white arrows). Brown and blue colours in IHC stains indicate positive staining against IL6, and hematoxylin counterstain, respectively.

Given that pSi degrades and releases both Si and B species, it is important to study the effect of those degradation products on distal organs. It has been reported that pSi

nanoparticles tend to accumulate in the liver and spleen when they are intravenously introduced into mice [53]. Therefore, the histology of liver and spleen was studied. Figure 7A shows the H&E staining of the liver and spleen of mice implanted with PCL, THC pSi and PITHC pSi rugate filters. Neither tissue necrosis nor obvious inflammatory cell infiltration were observed in the liver and spleen for either of these samples, indicating there was no acute toxicity to these organs. However, it is worth noting that there was an increase of Kupffer cells population in the THC pSi rugate filter group, around a central vein of the liver, which was not observed in the PCL or PITHC pSi rugate filter group (Figure 7A, arrows). There was no observable difference in the size of white pulps and red pulps in the spleen harvested from each group, indicating that the population of T-cells and B-cells were not significantly altered by the implanted materials (Figure 7A). These results collectively suggest that there was neither acute systemic inflammation nor tissue necrosis induced by any of the three samples in distal organs.

To investigate the structural and optical integrity of the implanted pSi rugate filters, the pore structures were first exposed by microtoming and were imaged under SEM. Figure 7B shows a cross-section of the nanostructure of a THC pSi rugate filter before implantation, and THC pSi and PITHC pSi explanted after 7 days. Both explanted pSi samples displayed parallel pore structures similar to the freshly etched sample, indicating that their structural integrity was maintained *in vivo*. We further demonstrated the optical signal reflected from a subcutaneous PITHC rugate filter, recorded through the skin. The skin around an implant was first stretched tight over the implant and a light probe was aligned manually with the implanted rugate filter (Figure 7C & D). Figure 7E shows that an implanted rugate filter which reflects light in the far-red range could be read clearly with low signal-noise ratio through the skin. Comparing the signal between an implanted and a water immersed, far-red rugate filter, there is a measurable red shift of the peak position. This effect arises due to the increase in refractive index from the water to the physiological fluid that the implanted rugate filter is in contact with. The *in vivo* signal of the far-red PITHC rugate filter was compared to the *in vivo* signal of a rugate filter with a shorter (~ 560 nm) peak position. In contrast to the far-red rugate filter, the signal from the shorter wavelength rugate filter displayed a low signal to noise ratio and could not be measured clearly. This may be due to the higher absorption of light at shorter wavelength by the tissue and fluid.

ACCEPTED MANUSCRIPT

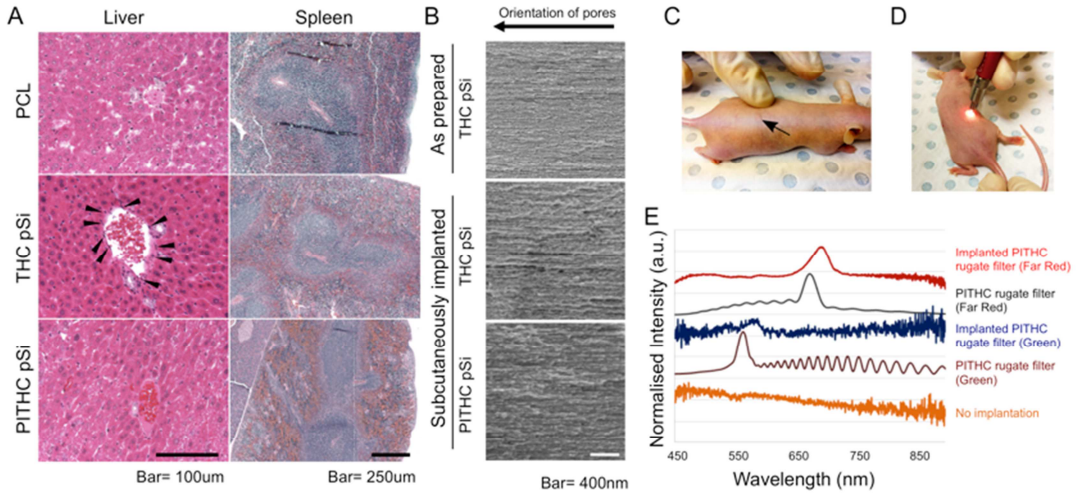

Figure 7: Optical functionality of subcutaneously implanted PITHC rugate filters and impact to distal organs. (A) H&E staining of liver and spleen. Arrows indicate increased proportion of Kupffer cells. (B) SEM images of the cross-section of subcutaneously implanted THC pSi and PITHC pSi, exposed by microtoming of skin tissue. An SEM image of THC pSi before implantation is shown for comparison. (C & D) Images showing the reading of the implanted PITHC pSi rugate filter through the skin of a skh:hr mouse. (E) Photonic peaks of "Green" and "Far Red" PITHC pSi rugate filter being read through the skin, along with the optical reflectance of these rugate filters immersed in water and the reflectance of a blank skin section. All *in vivo* spectra are backgrounded to the reflectance spectrum from a blank skin section.

4 Discussion

Intrinsic attributes of pSi, such as highly tuneable pore geometries and optical properties, have unlocked new possibilities for the use of this material in future and nanomedicine including in *ex vivo* (i.e. LOC) and *in vivo* (i.e. subcutaneous biosensor, smart drug delivery carrier) settings. However, for those applications, control of stability and biocompatibility of pSi materials is of utmost importance, and the biocompatible, implantable and optically functional rugate filter has never been perceived. Here, we first report in detail on a pSi rugate filter stabilised by THC, and demonstrate it as a potential biomaterial for constructing LOC and implantable subcutaneous biosensor. The effect of various surface treatments on the photonic properties and biocompatibility of the pSi rugate filters were then investigated and a methodology for mitigating cytotoxicity was devised. We further demonstrate, for the first time in the field, that this biocompatible rugate filter is optically functional in both *in vitro* LOC circumstance, and importantly, in a subcutaneous passive biosensing setting.

Several approaches have been studied to stabilise pSi structures, including hydrosilylation, thermal oxidation [19, 54] and hydrocarbonisation [4]. Recent work on the *in vivo* applications of pSi microparticles have focused on thermal oxidation and hydrocarbonisation surface functionalisations, with the material shown to be biocompatible and of sufficient stability in these forms [27, 55, 56]. Taking a similar approach on pSi rugate filters, we compared TO and THC functionalisation in terms of their stability in physiological buffers, by using optical reflectance and Si and B

species release as indicators. In accordance with existing studies [24], we found that THC modification was a better method for stabilising the pSi rugate filter for prolonged exposure to aqueous physiological conditions. TO pSi has been reported to perform well as a drug carriers [57, 58]. However, oxidation at 500-600 ˚C was found to be unsuccessful in stabilising the pSi rugate filter in physiological conditions for longer time periods. In turn, TO800 leads to immediate loss of the photonic properties. In contrast, the THC pSi rugate filter maintained its photonic properties throughout the entire study period of 16 days. Therefore, THC stabilisation is a promising method to enable long serving *in vivo* devices such as long-term smart drug release systems that self-report drug release dosage, or implantable biosensors to report on disease progression or treatment performance.

Despite the generally accepted paradigm that pSi, in particle form, is quite biocompatible, we discovered that p^{++} and n^{++} pSi rugate filters with TO or THC treatments, showed cytotoxicity in indirect culture, with the exception of TO800 treatment. We showed that the source of the observed cytotoxicity was the generation of ROS from the pSi materials. Indeed, the generation of ROS from pSi particles has been reported in a few studies [6, 59, 60] and the mechanism of the induction of cell necrosis and apoptosis by ROS has also been documented [61, 62]. In earlier work, we observed ROS generation from freshly etched pSi microparticles in the absence of light and showed that treatment of pSi microparticles *via* TO reduced the generation of ROS, and, at the same time, the cytotoxicity [6]. A follow up *in vivo* study by our group on TO stabilised pSi particles also demonstrated excellent biocompatibility of TO treated pSi with ocular tissue [5]. However, we show here that TO800 treatment of a pSi rugate filter fabricated using the current conditions abolishes the photonic properties (Figure 2C). Nevertheless, optimisation of the fabrication conditions to design a functional rugate suitable for TO800 treatment may be possible. To date, the relationship between the pSi nanostructure and ROS generation remains unclear. We speculate that the origin of ROS depends on the integrity of the superficial layer of the nanostructure, since we observed that the highly unstable as-etched pSi generated less ROS than the much more stable form of THC pSi (Figure S2E); coincidently, as-etched pSi rugate filter surface was less cytotoxic than TO and THC pSi. However, further in-depth investigation is necessary to investigate this phenomenon.

We investigated if the inherent cytotoxicity of a THC pSi rugate filter could be abolished. We demonstrated that the THC rugate filter surface, after pre-incubation for 10 days in DMEM, is not cytotoxic and supports the culture of fibroblasts similarly to conventional tissue culture surfaces. When fibroblasts were cultured on this surface, their phenotypes such as morphology, proliferation rate, and the deposition of collagen type 1 in the ECM were not affected. Similarly, Lu *et al*. reported that single layered pSi substrate, which was oxidised in de-ionised H_2O or DMEM, is able to support the culture of osteoblasts [63], although they did not report the involvement of ROS. It should also be highlighted that the PITHC pSi rugate filter, which was covered with a dense fibrotic matrix composed of fibroblast and extracellular matrixes, retained its structure and optical functionality, as indicated by its characteristic reflectance spectrum and the subsequent red shift in response to increasing sucrose concentrations (Figure 4D-F).

We propose that the pre-incubation of the THC pSi rugate filter is a robust method to dramatically improve its cytocompatibility, thus enabling a range of *in vitro*

applications. For example, pSi rugate filters have been coated with a transparent resin and applied as a smart cell culture platform to characterise cancer cells [64]. But the resin coating prevents the use of pSi as a transducer for example to enable the biosensing of pathogens [65]. The PITHC rugate filter surface reported in this study retains an open porous structure, available for functionalisation and detection. Therefore, we believe that the strategy reported in our study may lead to the development of a smart cell culture platform that enables real time, high throughput, single cell phenotypic characterisation to answer the need for cancer cells prognostic applications [66].

The improvement of the *in vitro* cytocompatibility of a pSi rugate filter prompted us to explore its *in vivo* performance in the form of an implant in a murine model. We demonstrated that the biocompatibility of the PITHC pSi rugate filter was improved dramatically compared to the THC pSi rugate filter. There was no sign of tissue necrosis or acute inflammation around PITHC pSi rugate filter implants. It was also observed that the wound healing, cellularity and tissue architecture around PITHC pSi rugate filter implants was virtually indistinguishable to PCL and Sham controls. In contrast, tissue around THC pSi rugate filter implants (without pre-incubation) appeared to be cyst-filled and necrotic with obvious inflammatory responses. Although there are limited *in vivo* investigations into the biocompatibility of pSi film implants, our observations coincide with some of the existing studies. For example TO treated pSi microparticles have been shown to be biocompatible as an ocular implant [5, 14] in consistence with our *in vitro* studies. Johansson *et al*. reported that nerve tissue around a pSi electrode was less dense than the tissue around a polished silicon implant [67]. This agrees with our observation that there was loss of cellularity for tissue around a THC pSi rugate filter, and the histology appeared to be filled with cysts. In terms of the acute inflammation that we observed around the THC pSi rugate filter, Tolli *et al*. found upregulation of IL-6 in tissues harvested from mice intravenously receiving THC pSi microparticles [68]. T-cell and B-cell populations in spleen were previously shown to be unaffected by the injection of THC pSi microparticles [7]. Consistent with this, we show that the histology of the spleen in mice carrying THC pSi rugate filter implant appeared normal. Shahbazi *et al.* also showed that intravenous administration of THC nanoparticles did not causes histological changes to liver, we observed an apparent increase in Kupffer cells around central veins in mice carrying THC rugate filter subcutaneously. Nevertheless, in general, no histologically changes were observed in the spleen and liver of mice carrying the PITHC implants, demonstrating the overall safety of the PITHC pSi rugate filter.

Prior to this study, there were very scarce reports demonstrating the challenge and the realisation of a non-invasive optical subcutaneous biosensor. Li *et al.* reported an attempt to measure the optical signal from a thermally oxidized pSi rugate filter through a piece of hand tissue with minimal success due to low signal to noise ratio[69]. Their report has not even revealed the stability and biocompatibility of the rugate filter. Similarly, we recently documented the comparison of different pSi optical filters in terms of signal clarity using an *in vitro* platform[15]. The scarcity in existing evidence may due to the lack of chemical stabilisation methods for the pSi material. We demonstrated, for the first time, a stable and biocompatible pSi rugate filter that also possesses optical functionality in cell culture and subcutaneous setting. Unlike the existing reports available, the optical signals could be read though the skin

of living mice with clarity after 1 week post-implantation. The red shift observed after implantation also implicates its optical functionality. This optical functionality is possibly very useful in realising a self-reporting drug release implant to reveal the amount of drug released from the porous layer via an optical peak shift in real-time. Of course, changes in the physiological environment around the implant may lead to drift in the sensor response which will need to be taken into account for example by splitting the sensor into a control patch and a sensor patch [70, 71]. To enable subcutaneous biosensing of specific biomolecules, future studies need to be carried out by studying the performance and challenge associated with the use of receptor-functionalized PITHC rugate filters, in *in vivo* scenarios

5 Conclusion

The unique optical functionalities of pSi rugate filters are thought to be game changing in future medicine, by enabling LOC and *in vivo* passive biosensing applications. However, the limited stability of pSi in physiological conditions, surprising scarcity of existing knowledge on its *in vivo* biocompatibility, and on the feasibility of its optical signal being read through tissues has hindered such development. Here, we investigated and delineated the cause of the biocompatibility issues associated with THC pSi rugate filter surfaces. Then, strategies to mitigate this undesired cytotoxicity, as well as to stabilise the pSi structure in terms of its optical reflectance were developed, interrogated and discussed. We demonstrated that PITHC pSi rugate filter surfaces are highly cytocompatible *in vitro*, and also biocompatible *in vivo*. As both the lifetime/stability and biocompatibility of PITHC pSi rugate filters are greatly enhanced, we also demonstrated the optical functionalities of this rugate filter in a cell culture and subcutaneous setting. We believe that this study may foster the translation of pSi-based materials into *in vitro* LOC, long-term self-reporting drug delivery, and *in vivo* biosensing applications.

Acknowledgement:

PregTech Pty Ltd. funded this study but had no involvement in study design, data collection, data analysis, data interpretation, and the writing of the report.

ACCEPTED MANUSCRIPT

References:

[1] Barnes TJ, Jarvis KL, Prestidge CA. Recent advances in porous silicon technology for drug delivery. Therapeutic delivery. 2013;4:811-23.
[2] Anderson SHC, Elliott H, Wallis DJ, Canham LT, Powell JJ. Dissolution of different forms of partially porous silicon wafers under simulated physiological conditions. physica status solidi (a). 2003;197:331-5.
[3] Rico H, Gallego-Lago JL, Hernandez ER, Villa LF, Sanchez-Atrio A, Seco C, et al. Effect of silicon supplement on osteopenia induced by ovariectomy in rats. Calcif Tissue Int. 2000;66:53-5.
[4] Bimbo LM, Sarparanta M, Santos HA, Airaksinen AJ, Mäkilä E, Laaksonen T, et al. Biocompatibility of Thermally Hydrocarbonized Porous Silicon Nanoparticles and their Biodistribution in Rats. ACS Nano. 2010;4:3023-32.
[5] Low SP, Voelcker NH, Canham LT, Williams KA. The biocompatibility of porous silicon in tissues of the eye. Biomaterials. 2009;30:2873–80.
[6] Low SP, Williams KA, Canham LT, Voelcker NH. Generation of reactive oxygen species from porous silicon microparticles in cell culture medium. J Biomed Mater Res A. 2010;93:1124-31.
[7] Shahbazi MA, Hamidi M, Makila EM, Zhang H, Almeida PV, Kaasalainen M, et al. The mechanisms of surface chemistry effects of mesoporous silicon nanoparticles on immunotoxicity and biocompatibility. Biomaterials. 2013;34:7776-89.
[8] Coffer JL, Whitehead MA, Nagesha DK, Mukherjee P, Akkaraju G, Totolici M, et al. Porous silicon-based scaffolds for tissue engineering and other biomedical applications. physica status solidi (a). 2005;202:1451-5.
[9] Bimbo LM, Mäkilä E, Laaksonen T, Lehto V-P, Salonen J, Hirvonen J, et al. Drug permeation across intestinal epithelial cells using porous silicon nanoparticles. Biomaterials. 2011;32:2625-33.
[10] Osminkina LA, Sivakov VA, Mysov GA, Georgobiani VA, Natashina Ucapital A C, Talkenberg F, et al. Nanoparticles prepared from porous silicon nanowires for bio-imaging and sonodynamic therapy. Nanoscale research letters. 2014;9:463.
[11] Pacholski C. Photonic crystal sensors based on porous silicon. Sensors. 2013;13:4694-713.
[12] Li S, Hu D, Huang J, Cai L. Optical sensing nanostructures for porous silicon rugate filters. Nanoscale research letters. 2012;7:79.
[13] Lin VS, Motesharei K, Dancil KP, Sailor MJ, Ghadiri MR. A porous silicon-based optical interferometric biosensor. Science. 1997;278:840-3.
[14] Cheng L, Anglin E, Cunin F, Kim D, Sailor MJ, Falkenstein I, et al. Intravitreal properties of porous silicon photonic crystals: a potential self-reporting intraocular drug-delivery vehicle. The British journal of ophthalmology. 2008;92:705-11.
[15] Acquaroli LN, Kuchel T, Voelcker NH. Towards implantable porous silicon biosensors. RSC Advances. 2014;4:34768-73.
[16] Gupta B, Zhu Y, Guan B, Reece PJ, Gooding JJ. Functionalised porous silicon as a biosensor: emphasis on monitoring cells in vivo and in vitro. Analyst. 2013;138:3593-615.
[17] Stefano LD, Rotiroti L, Rea I, Tommasi ED, Vitale A, Rossi M, et al. Design and realization of highly stable porous silicon optical biosensor based on proteins from extremophiles2007.

[18] Stewart MP, Robins EG, Geders TW, Allen MJ, Cheul Choi H, Buriak JM. Three Methods for Stabilization and Functionalization of Porous Silicon Surfaces via Hydrosilylation and Electrografting Reactions. physica status solidi (a). 2000;182:109-15.
[19] Hecini M, Khelifa A, Bouzid B, Drouiche N, Aoudj S, Hamitouche H. Study of formation, stabilization and properties of porous silicon and porous silica. Journal of Physics and Chemistry of Solids. 2013;74:1227-34.
[20] McInnes SJP, Irani Y, Williams KA, Voelcker NH. Controlled drug delivery from composites of nanostructured porous silicon and poly(L-lactide). Nanomedicine. 2012;7:995-1016.
[21] Krismastuti FSH, Pace S, Voelcker NH. Porous Silicon Resonant Microcavity Biosensor for Matrix Metalloproteinase Detection. Advanced Functional Materials. 2014;24:3639-50.
[22] Sweetman MJ, Ronci M, Ghaemi SR, Craig JE, Voelcker NH. Porous Silicon Films Micropatterned with Bioelements as Supports for Mammalian Cells. Advanced Functional Materials. 2012;22:1158-66.
[23] Sweetman MJ, Shearer CJ, Shapter JG, Voelcker NH. Dual Silane Surface Functionalization for the Selective Attachment of Human Neuronal Cells to Porous Silicon. Langmuir. 2011;27:9497-503.
[24] Jalkanen T, Torres-Costa V, Mäkilä E, Kaasalainen M, Koda R, Sakka T, et al. Selective Optical Response of Hydrolytically Stable Stratified Si Rugate Mirrors to Liquid Infiltration. ACS Applied Materials & Interfaces. 2014;6:2884-92.
[25] Salonen J, Björkqvist M, Laine E, Niinistö L. Stabilization of porous silicon surface by thermal decomposition of acetylene. Applied Surface Science. 2004;225:389-94.
[26] Wang C-F, Mäkilä EM, Bonduelle C, Rytkönen J, Raula J, Almeida S, et al. Functionalization of Alkyne-Terminated Thermally Hydrocarbonized Porous Silicon Nanoparticles With Targeting Peptides and Antifouling Polymers: Effect on the Human Plasma Protein Adsorption. ACS Applied Materials & Interfaces. 2014;7:2006-15.
[27] Rytkönen J, Miettinen R, Kaasalainen M, Lehto V-P, Salonen J, Närvänen A. Functionalization of Mesoporous Silicon Nanoparticles for Targeting and Bioimaging Purposes. Journal of Nanomaterials. 2012;2012:9.
[28] Ariza-Avidad M, Nieto A, Salinas-Castillo A, Capitan-Vallvey LF, Miskelly GM, Sailor MJ. Monitoring of degradation of porous silicon photonic crystals using digital photography.
[29] A. Kovacs PJ, X. Y. Meng and U. Mescheder. Characterization of porous silicon based optical sensor system for biosensor applications. Sensors. Christchurch: IEEE; 2009. p. 21 - 6.
[30] Sciacca B, Secret E, Pace S, Gonzalez P, Geobaldo F, Quignard F, et al. Chitosan-functionalized porous silicon optical transducer for the detection of carboxylic acid-containing drugs in water. Journal of Materials Chemistry. 2011;21:2294-302.
[31] Chamard V, Dolino G, Muller F. Origin of a parasitic surface film on p+ type porous silicon. Journal of Applied Physics. 1998;84:6659-66.
[32] Rello S, Stockert JC, Moreno V, Gamez A, Pacheco M, Juarranz A, et al. Morphological criteria to distinguish cell death induced by apoptotic and necrotic treatments. Apoptosis : an international journal on programmed cell death. 2005;10:201-8.

[33] Pal AK, Bello D, Budhlall B, Rogers E, Milton DK. Screening for Oxidative Stress Elicited by Engineered Nanomaterials: Evaluation of Acellular DCFH Assay. Dose-response : a publication of International Hormesis Society. 2012;10:308-30.
[34] Myhre O, Andersen JM, Aarnes H, Fonnum F. Evaluation of the probes 2',7'-dichlorofluorescin diacetate, luminol, and lucigenin as indicators of reactive species formation. Biochemical pharmacology. 2003;65:1575-82.
[35] Jingkun Jiang GnOr, Alison Elder, Robert Gelein, Pamela Mercer, Pratim Biswas. Does Nanoparticle Activity Depend upon Size and Crystal Phase? Nanotoxicology. 2008;2:33–42.
[36] Foucaud L, Wilson MR, Brown DM, Stone V. Measurement of reactive species production by nanoparticles prepared in biologically relevant media. Toxicology letters. 2007;174:1-9.
[37] Chen CZ, Raghunath M. Focus on collagen: in vitro systems to study fibrogenesis and antifibrosis state of the art. Fibrogenesis Tissue Repair. 2009;2:7.
[38] Fish PV, Allan GA, Bailey S, Blagg J, Butt R, Collis MG, et al. Potent and selective nonpeptidic inhibitors of procollagen C-proteinase. J Med Chem. 2007;50:3442-56.
[39] Shtenberg G, Massad-Ivanir N, Fruk L, Segal E. Nanostructured Porous Si Optical Biosensors: Effect of Thermal Oxidation on Their Performance and Properties. ACS Applied Materials & Interfaces. 2014.
[40] Janshoff A, Dancil KPS, Steinem C, Greiner DP, Lin VSY, Gurtner C, et al. Macroporous p-Type Silicon Fabry-Perot Layers. Fabrication, Characterization, and Applications in Biosensing J Am Chem Soc. 1998;120:12108 - 16.
[41] Sweetman MJ, Harding FJ, Graney SD, Voelcker NH. Effect of oligoethylene glycol moieties in porous silicon surface functionalisation on protein adsorption and cell attachment. Appl Surf Sci. 2011;257:6768-74
[42] Wojtyk JTC, Morin KA, Boukherroub R, Wayner DDM. Modification of Porous Silicon Surfaces with Activated Ester Monolayers. Langmuir. 2002;18:6081-7.
[43] Sweetman MJ, McInnes SJP, Vasani RB, Guinan T, Blencowe A, Voelcker NH. Rapid, metal-free hydrosilanisation chemistry for porous silicon surface modification. Chemical Communications. 2015;51:10640-3.
[44] Vasin A, Okholin P, Verovsky I, Nazarov A, Lysenko V, Kholostov K, et al. Study of the processes of carbonization and oxidation of porous silicon by Raman and IR spectroscopy. Semiconductors. 2011;45:350-4.
[45] Jalkanen T, Mäkilä E, Sakka T, Salonen J, Ogata YH. Thermally promoted addition of undecylenic acid on thermally hydrocarbonized porous silicon optical reflectors. Nanoscale Research Letters. 2012;7:1-6.
[46] Robbie K, Cui Y, Elliott C, Kaminska K. Oxidation of evaporated porous silicon rugate filters. Applied Optics. 2006;45:8298-303.
[47] Astrova EV, Tolmachev VA. Effective refractive index and composition of oxidized porous silicon films. Materials Science and Engineering: B. 2000;69-70:142–8.
[48] Reddig PJ, Juliano RL. Clinging to life: cell to matrix adhesion and cell survival. Cancer metastasis reviews. 2005;24:425-39.
[49] Kocgozlu L, Lavalle P, Koenig G, Senger B, Haikel Y, Schaaf P, et al. Selective and uncoupled role of substrate elasticity in the regulation of replication and transcription in epithelial cells. Journal of cell science. 2010;123:29-39.
[50] McDougall S, Dallon J, Sherratt J, Maini P. Fibroblast migration and collagen deposition during dermal wound healing: mathematical modelling and clinical

implications. Philosophical transactions Series A, Mathematical, physical, and engineering sciences. 2006;364:1385-405.
[51] Briso EM, Guinea-Viniegra J, Bakiri L, Rogon Z, Petzelbauer P, Eils R, et al. Inflammation-mediated skin tumorigenesis induced by epidermal c-Fos. Genes & development. 2013;27:1959-73.
[52] Volk SW, Wang Y, Mauldin EA, Liechty KW, Adams SL. Diminished type III collagen promotes myofibroblast differentiation and increases scar deposition in cutaneous wound healing. Cells Tissues Organs. 2011;194:25-37.
[53] Park JH, Gu L, von Maltzahn G, Ruoslahti E, Bhatia SN, Sailor MJ. Biodegradable luminescent porous silicon nanoparticles for in vivo applications. Nat Mater. 2009;8:331-6.
[54] Aggarwal G, Mishra P, Joshi B, Harsh, Islam SS. Porous silicon surface stability: a comparative study of thermal oxidation techniques. Journal of Porous Materials. 2014;21:23-9.
[55] Liu D, Mäkilä E, Zhang H, Herranz B, Kaasalainen M, Kinnari P, et al. Nanostructured Porous Silicon-Solid Lipid Nanocomposite: Towards Enhanced Cytocompatibility and Stability, Reduced Cellular Association, and Prolonged Drug Release. Advanced Functional Materials. 2013;23:1893-902.
[56] Gu L, Ruff LE, Qin Z, Corr M, Hedrick SM, Sailor MJ. Multivalent Porous Silicon Nanoparticles Enhance the Immune Activation Potency of Agonistic CD40 Antibody. Advanced Materials. 2012;24:3981-7.
[57] Vasani RB, McInnes SJP, Cole MA, Jani AMM, Ellis AV, Voelcker NH. Stimulus-Responsiveness and Drug Release from Porous Silicon Films ATRP-Grafted with Poly(N-isopropylacrylamide). Langmuir. 2011;27:7843–53.
[58] McInnes SJP, Voelcker NH. Silicon-polymer hybrid materials for drug delivery. Future Med Chem. 2009;1:1051-74.
[59] Santos HA, Riikonen J, Salonen J, Makila E, Heikkila T, Laaksonen T, et al. In vitro cytotoxicity of porous silicon microparticles: effect of the particle concentration, surface chemistry and size. Acta Biomater. 2010;6:2721-31.
[60] Mori M, Almeida PV, Cola M, Anselmi G, Makila E, Correia A, et al. In vitro assessment of biopolymer-modified porous silicon microparticles for wound healing applications. European journal of pharmaceutics and biopharmaceutics : official journal of Arbeitsgemeinschaft fur Pharmazeutische Verfahrenstechnik eV. 2014;88:635-42.
[61] Teramoto S, Tomita T, Matsui H, Ohga E, Matsuse T, Ouchi Y. Hydrogen peroxide-induced apoptosis and necrosis in human lung fibroblasts: protective roles of glutathione. Japanese journal of pharmacology. 1999;79:33-40.
[62] Boonstra J, Post JA. Molecular events associated with reactive oxygen species and cell cycle progression in mammalian cells. Gene. 2004;337:1-13.
[63] Yang Y YL, Cai L. Osteoblast adhesion on porous silicon. Bulletin of Advanced Technology Research. 2009;3:25-8.
[64] Schwartz MP, Derfus AM, Alvarez SD, Bhatia SN, Sailor MJ. The Smart Petri Dish: A Nanostructured Photonic Crystal for Real-Time Monitoring of Living Cells. Langmuir. 2006;22:7084-90.
[65] Massad-Ivanir N, Shtenberg G, Segal E. Optical detection of E. coli bacteria by mesoporous silicon biosensors. Journal of visualized experiments : JoVE. 2013:e50805.
[66] Bohunicky B, Mousa SA. Biosensors: the new wave in cancer diagnosis. Nanotechnology, science and applications. 2010;4:1-10.

ACCEPTED MANUSCRIPT

[67] Johansson F, Wallman L, Danielsen N, Schouenborg J, Kanje M. Porous silicon as a potential electrode material in a nerve repair setting: Tissue reactions. Acta Biomaterialia. 2009;5:2230-7.
[68] Tolli MA, Ferreira MP, Kinnunen SM, Rysa J, Makila EM, Szabo Z, et al. In vivo biocompatibility of porous silicon biomaterials for drug delivery to the heart. Biomaterials. 2014;35:8394-405.
[69] Li YY, Cunin F, Link JR, Gao T, Betts RE, Reiver SH, et al. Polymer replicas of photonic porous silicon for sensing and drug delivery applications. Science. 2003;299:2045-7.
[70] Sweetman MJ, Voelcker NH. Chemically patterned porous silicon photonic crystals towards internally referenced organic vapour sensors. RSC Advances. 2012;2:4620-2.
[71] Ruminski AM, Barillaro G, Chaffin C, Sailor MJ. Internally Referenced Remote Sensors for HF and Cl2 Using Reactive Porous Silicon Photonic Crystals. Adv Funct Mater. 2011;21:1511-25.

ACCEPTED MANUSCRIPT

Supplementary Figures:

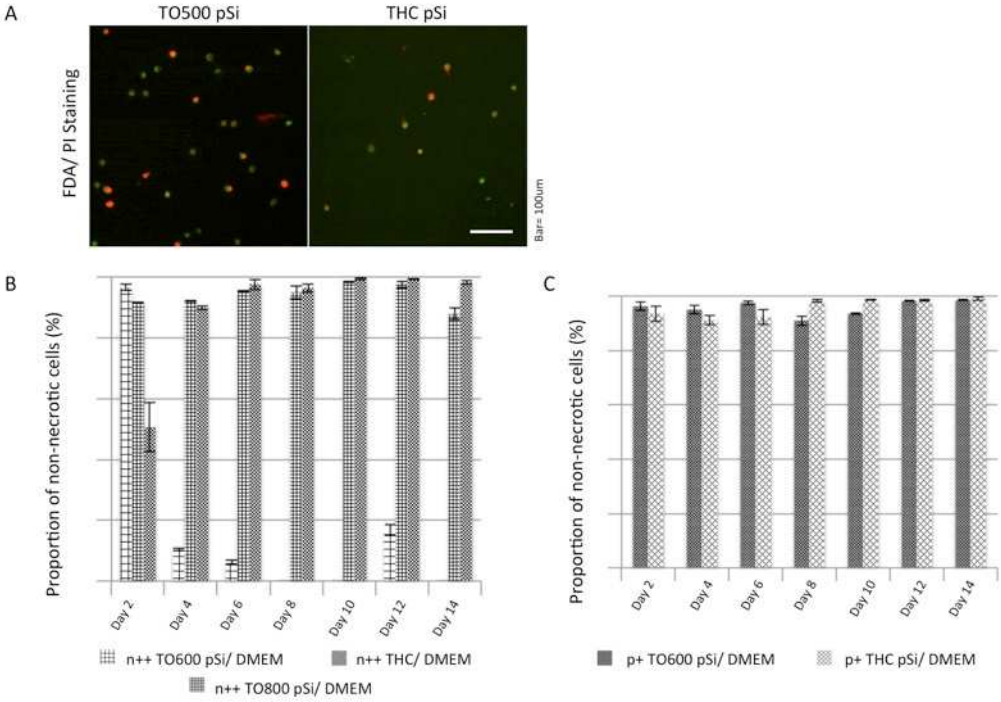

Figure S1: (A) FDA/ PI staining of fibroblasts cultured on TO500 pSi and THC pSi surfaces. (B) Cytotoxicity of degradation products from differently treated highly doped n-type and (C) p-type pSi rugate filters collected at different time points. This is reported in terms of the proportion of non-necrotic cells (%).

ACCEPTED MANUSCRIPT

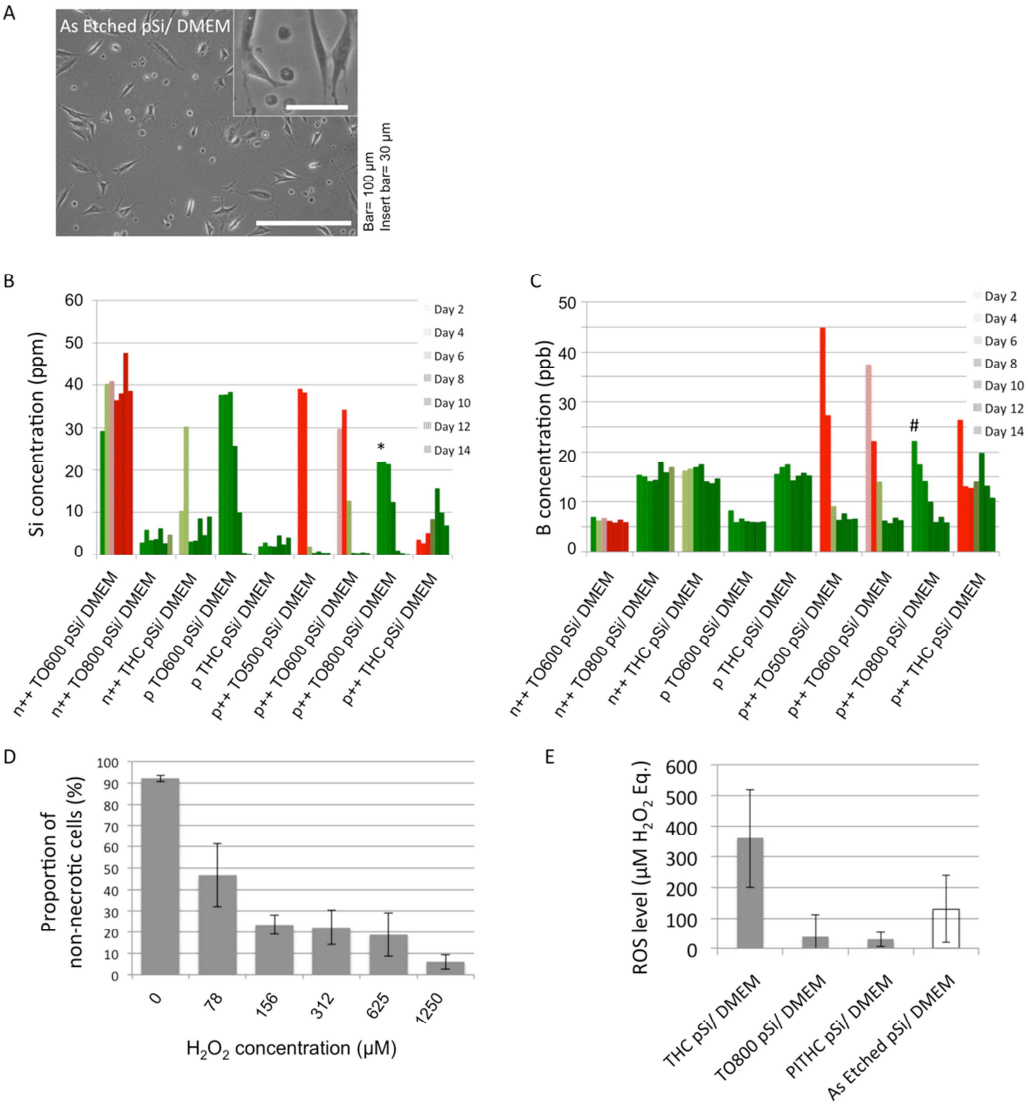

Figure S2: (A) Morphology of fibroblasts after 24 h exposure to degradation products of as-etched pSi in DMEM (as-etched pSi/DMEM) (B&C) Colour-coded ICP-MS quantification of Si and B ion dissolution from all pSi surfaces. Cytocompatibility index is colour coded such that, green: 80-100 %, light green: 50-80 %, pale red: 20-50 % and red: 0-20 %. (D) Viability of NIH3T3 exposed to various concentrations of H_2O_2 reported in terms of the proportion of non-necrotic cells (%) (E). Comparison of ROS level between As Etched pSi, and THC, TO800 and PITHC pSi rugate filters, reported as H2O2 equivalents (µM).